

# Probing the myelin water compartment with a saturation-recovery, multi-echo gradient-recalled echo sequence

Elena Kleban<sup>1,2</sup>  | Penny Gowland<sup>1</sup> | Richard Bowtell<sup>1</sup>  

<sup>1</sup>Sir Peter Mansfield Imaging Centre, School of Physics and Astronomy, University of Nottingham, Nottingham, UK

<sup>2</sup>Cardiff University Brain Research Imaging Centre, School of Psychology, Cardiff University, Cardiff, UK

## Correspondence

Richard Bowtell, Sir Peter Mansfield Imaging Centre, School of Physics and Astronomy, University of Nottingham, University Park, NG7 2RD, Nottingham, UK.

Email: Richard.Bowtell@nottingham.ac.uk

**Purpose:** To investigate the effect of varying levels of  $T_1$ -weighting on the evolution of the complex signal from white matter in a multi-echo gradient-recalled echo (mGRE) saturation-recovery sequence.

**Theory and Methods:** Analysis of the complex signal evolution in an mGRE sequence allows the contributions from short- and long- $T_2^*$  components to be separated, thus providing a measure of the relative strength of signals from the myelin water, and the external and intra-axonal compartments. Here we evaluated the effect of different levels of  $T_1$ -weighting on these signals, expecting that the previously reported, short  $T_1$  of the myelin water would lead to a relative enhancement of the myelin water signal in the presence of signal saturation. Complex, saturation-recovery mGRE data from the splenium of the corpus callosum from 5 healthy volunteers were preprocessed using a frequency difference mapping (FDM) approach and analyzed using the 3-pool model of complex signal evolution in white matter.

**Results:** An increase in the apparent  $T_1$  as a function of echo time was demonstrated, but this increase was an order of magnitude smaller than that expected from previously reported myelin water  $T_1$ -values. This suggests the presence of magnetization transfer and exchange effects which counteract the  $T_1$ -weighting.

**Conclusion:** Variation of the  $B_1^+$  amplitude in a saturation-recovery mGRE sequence can be used to modulate the relative strength of signals from the different compartments in white matter, but the modulation is less than predicted from previously reported  $T_1$ -values.

## KEYWORDS

3-pool model, frequency difference mapping, magnetic susceptibility, myelin water, saturation recovery

This is an open access article under the terms of the Creative Commons Attribution License, which permits use, distribution and reproduction in any medium, provided the original work is properly cited.

© 2021 The Authors. *Magnetic Resonance in Medicine* published by Wiley Periodicals LLC on behalf of International Society for Magnetic Resonance in Medicine.

## 1 | INTRODUCTION

White matter microstructure can be probed using gradient echo techniques, which are sensitive to the variations of NMR signal frequency produced within and across the different compartments by the myelin sheath. Because of its extremely short  $T_2^*$  relaxation time,<sup>1</sup> the signal from myelin itself is not directly detectable using conventional MRI pulse sequences, but the signal from the water trapped within the myelin sheath provides a sensitive marker of the presence of myelin. The myelin water (MW) signal shows relatively rapid  $T_2^*$  relaxation and also experiences a frequency offset that depends on the orientation of the sheath relative to the  $\vec{B}_0$ -field. The sheath also produces a smaller orientation-dependent frequency offset of opposite sign inside the axon and a spatially varying field outside. These field variations are largest when the nerve fibers are oriented perpendicular to  $\vec{B}_0$  and their magnitude also depends on the axon geometry and on the isotropic and anisotropic susceptibility of the lipid chains forming the myelin sheath.

As a result of these effects, analysis of the evolution of the phase and magnitude of the gradient echo signal from white matter allows the signal contributions from the different compartments to be separated out, and potentially provides a new method of probing microstructure. This is best done by using a multi-echo gradient-recalled echo (mGRE) sequence. The phase carries important information in this analysis since it is sensitive to the sign of the frequency offsets. However, the phase variation resulting from the differences in the evolution of the signals from the different white matter compartments, which is sensitive to local microstructure, is swamped by nonlocal effects due to larger length-scale magnetic field inhomogeneities, RF-related phase offsets, physiological fluctuations, and eddy current-related field perturbations. A robust method for removing the nonlocal field perturbation effects, which does not corrupt the local signal evolution is needed to access the effects of microstructure on the phase.<sup>2-6</sup> Frequency difference mapping (FDM) uses the phase information from the first and second echoes of a multi-echo dataset to eliminate any phase effects that are constant or linearly varying with time down the echo train, leaving only phase offsets which result from a variation of apparent frequency with echo time, such as those due to microstructural compartmentalization.<sup>6</sup> Scaling the remaining phase by the difference in echo time from the time of the second echo, then produces a frequency difference measure. As a result of the rapid decay of the MW signal and its positive resonance frequency offset (which is strongest for fibers perpendicular to  $\vec{B}_0$ ), we expect the frequency difference to be negative at longer echo times and the FDM contrast to increase with echo time while the MW signal is present.

Here, we apply the FDM approach to the signals produced using a saturation-recovery, mGRE sequence, applied to the

human corpus callosum with a fixed short repetition time and variable excitation angle, to evaluate the evolution of longitudinal magnetization in the different white matter compartments. A variety of recent studies have investigated the complex evolution of longitudinal magnetization in white matter,<sup>7-11</sup> leading to the suggestion that there is a short  $T_1$ -component in the signal from white matter partially associated with the myelin water.<sup>12-17</sup> We therefore hypothesized that the short  $T_1$  of myelin water would lead to a relative increase of its contribution to the total signal with increasing flip angle in a saturation-recovery sequence with a fixed repetition time, and that increasing the level of saturation in this way would lead to a significant increase in the FDM contrast. By analyzing the evolution of the magnitude and FDM signals as a joint function of TE and flip angle, we also aimed to characterize the differences in longitudinal relaxation rate in the different compartments.

## 2 | THEORY

### 2.1 | Complex signal evolution in a bipolar mGRE sequence

In this work, we used a bipolar mGRE readout to be able to achieve a shorter echo spacing compared to that attainable with a monopolar readout. However, the phase of the complex mGRE signal acquired using bipolar readout gradients is inconsistent between the adjacent echoes due to eddy current effects. Particularly, the signal can be expressed as,<sup>18-22</sup>

$$S_n^\pm \equiv S^\pm(\vec{r}, TE_n) \sim S_0(\vec{r}) \cdot e^{i\Omega(\vec{r})TE_n} \cdot e^{i\phi_0(\vec{r})} \cdot e^{\pm(-1)^n i\psi_n} \cdot F(\vec{r}, TE_n) . \quad (1)$$

Here,  $F(\vec{r}, TE_n)$  is the multiexponential signal (described in the following section) measured at the  $n$ th gradient-echo time  $TE_n = TE_1 + (n - 1)\Delta TE$ , where  $TE_1$  is the first echo time and  $\Delta TE$  is the echo spacing. The frequency  $\Omega$  represents the effect of large length-scale field perturbations, which are predominantly induced by the magnetic susceptibility differences within the sample/subject, particularly those between brain tissue and air. The phase  $\phi_0$  describes static phase offsets such as those due to RF effects. The  $\pm$  sign indicates the polarity of the read gradient used in acquiring the first gradient echo.  $S_n^+$  and  $S_n^-$  thus correspond to the signals acquired at the same echo time, but with read gradient waveforms of opposite polarity. The phase  $\psi_n$  characterizes phase differences between echoes acquired under a positive or negative read gradient, including the effects of spatiotemporally varying field perturbations due to eddy currents, which change in sign, but not in absolute value, depending on the read gradient polarity. In a bipolar mGRE sequence, the phases  $\psi_n$  and  $\psi_{n+1}$  of the adjacent echoes  $n$  and  $n + 1$  will appear with opposite signs and will result in phase inconsistencies between these echoes.

Complex multiplication of  $S_n^+$  by  $S_n^-$  removes phase shifts due to  $\psi_n$  without corrupting the local signal evolution:

$$S_n^+ \cdot S_n^- = e^{i2\Omega TE_n} \cdot e^{i2\phi_0} \cdot [F_n]^2. \quad (2)$$

The subsequent calculation of a frequency difference map<sup>6</sup> from the combined signal  $S_n^+ \cdot S_n^-$  allows us to remove the RF-related phase offsets and the effects of large length-scale field perturbations without perturbing the local multiexponential signal, since:

$$[S_n^+ \cdot S_n^-]'' = \frac{S_n^+ \cdot S_n^- \cdot [S_1^+ \cdot S_1^-]^{n-2}}{[S_2^+ \cdot S_2^-]^{n-1}} = \left[ \frac{F_n \cdot [F_1]^{n-2}}{[F_2]^{n-1}} \right]^2. \quad (3)$$

The phase of the above expression can be scaled by the echo time to produce a frequency difference measure in Hz:

$$\text{FDM}_n = \frac{\arg([S_n^+ \cdot S_n^-]'')}{4\pi[n-2]\Delta TE}. \quad (4)$$

Other nonlocal and temporally nonlinear effects coming from other sources of eddy currents, for example, from the slice selective gradients, can be approximated at each echo time by a low-degree spatial polynomial.

## 2.2 | Modeling local WM signal evolution

The evolution of the complex mGRE signal from white matter can be described by using a simple 3-pool model,<sup>2,3,23,24</sup> where the signal evolution within the imaging voxel can be described as a sum of the signals from each of the water pools given by  $F_k(t) \sim A_k \cdot \exp(i\omega_k t) \cdot \exp(-R_{2,k}^* t)$ :

$$F(t) \sim \sum_k A_k \cdot e^{i\omega_k t} \cdot e^{-R_{2,k}^* t}. \quad (5)$$

$A_k$  is the signal fraction of each water pool,  $\omega_k$  denotes its angular frequency offset relative to a reference frequency, and  $R_{2,k}^*$  is its effective transverse relaxation rate. The subscript  $k$  indicates 1 of 3 water pools: e, a, and m stand for the extra-axonal, intra-axonal, and MW pools, respectively. Typical 3-pool model parameters for a fiber-oriented perpendicular to  $\vec{B}_0$  are listed in the table in Figure 1A.<sup>2,3,6,25</sup> The evolution of frequency difference with echo time is shown in the same figure (Figure 1B, red curve).

The signal fraction  $A_k$  for the pool  $k$  is proportional to the volume fraction  $V_k$  and proton density  $\rho_k$  for the compartment, and a longitudinal relaxation rate-dependent factor  $L_k$  (ie,  $A_k = V_k \rho_k L_k$ ). The volume fraction and proton density are independent of the scanning parameters and their combined effect can be described by a constant,  $c_k = V_k \rho_k$ , but the factor

$L_k$  will vary with the RF excitation amplitude, which defines the excitation flip angle  $\alpha$ , and also depends on the fixed repetition time, TR,

$$A_k(\alpha) = c_k \cdot L_k(\alpha) = \sin \alpha \cdot \frac{1 - e^{-TR/T_{1,k}}}{1 - \cos \alpha \cdot e^{-TR/T_{1,k}}}. \quad (6)$$

Here, we assumed that the longitudinal relaxation times of the intra- and extra-axonal water pools are similar and much longer than the repetition time: that is,  $T_{1,e} \approx T_{1,a} \gg TR$ , so that  $L_e(\alpha) = L_a(\alpha) = L_{\text{long}}(\alpha)$ . We also set the reference frequency equal to the Larmor frequency of the extra-axonal pool, so that  $\omega_e = 0$ .

Based on these assumptions, the local signal evolution from white matter can be described by the following expression:

$$F(\text{TE}_n, \alpha) \sim L_{\text{long}}(\alpha) \left( c_e \cdot e^{-R_{2,e}^* \text{TE}_n} + c_a \cdot e^{i\omega_a \text{TE}_n} \cdot e^{-R_{2,a}^* \text{TE}_n} \right) + c_m L_{\text{short}}(\alpha) \cdot e^{i\omega_m \text{TE}_n} \cdot e^{-R_{2,m}^* \text{TE}_n}. \quad (7)$$

We will refer to  $T_{1,e} \approx T_{1,a}$  values as  $T_{1,\text{long}}$  and to  $T_{1,m}$ -values as  $T_{1,\text{short}}$ .

## 3 | METHODS

### 3.1 | Data acquisition

The study was approved by the local ethics committee and subjects participated having given informed consent. Mid-sagittal, single-slice, RF-, and gradient-spoiled mGRE image data were acquired from 5 healthy subjects ( $24.2 \pm 0.7$  y, 3 female) on a 7T system (Achieva, Philips Healthcare, Netherlands). This mid-sagittal slice was selected as it cuts through the corpus callosum, which is a bundle of white matter fibers that connects the 2 hemispheres of the brain so that the fiber orientation is approximately perpendicular to the  $\vec{B}_0$ -field of the scanner when the subject is supine. As a result, the frequency offsets between the extra-, intra-axonal, and MW pools are maximized.<sup>2,3</sup> The in-plane resolution was  $1 \times 1 \text{ mm}^2$  and the slice thickness was 5 mm. We chose a single slice acquisition with a relatively large slice thickness to maximize the signal-to-noise ratio (SNR) in individual acquisitions and to allow repeated image acquisitions in a reasonable total experimental time for error characterization.

The read gradient was applied in the foot-head direction. Each protocol involved acquisition of 60 mGRE scans: spanning acquisitions with 6 different excitation angles, each repeated 10 times with the polarity of the bipolar read gradients reversed for half the acquisitions. To achieve different excitation angles, the amplitude of the RF pulse was varied while maintaining a fixed pulse length. The maximum  $B_1^+$ -amplitude and the pulse duration were defined by identifying the shortest

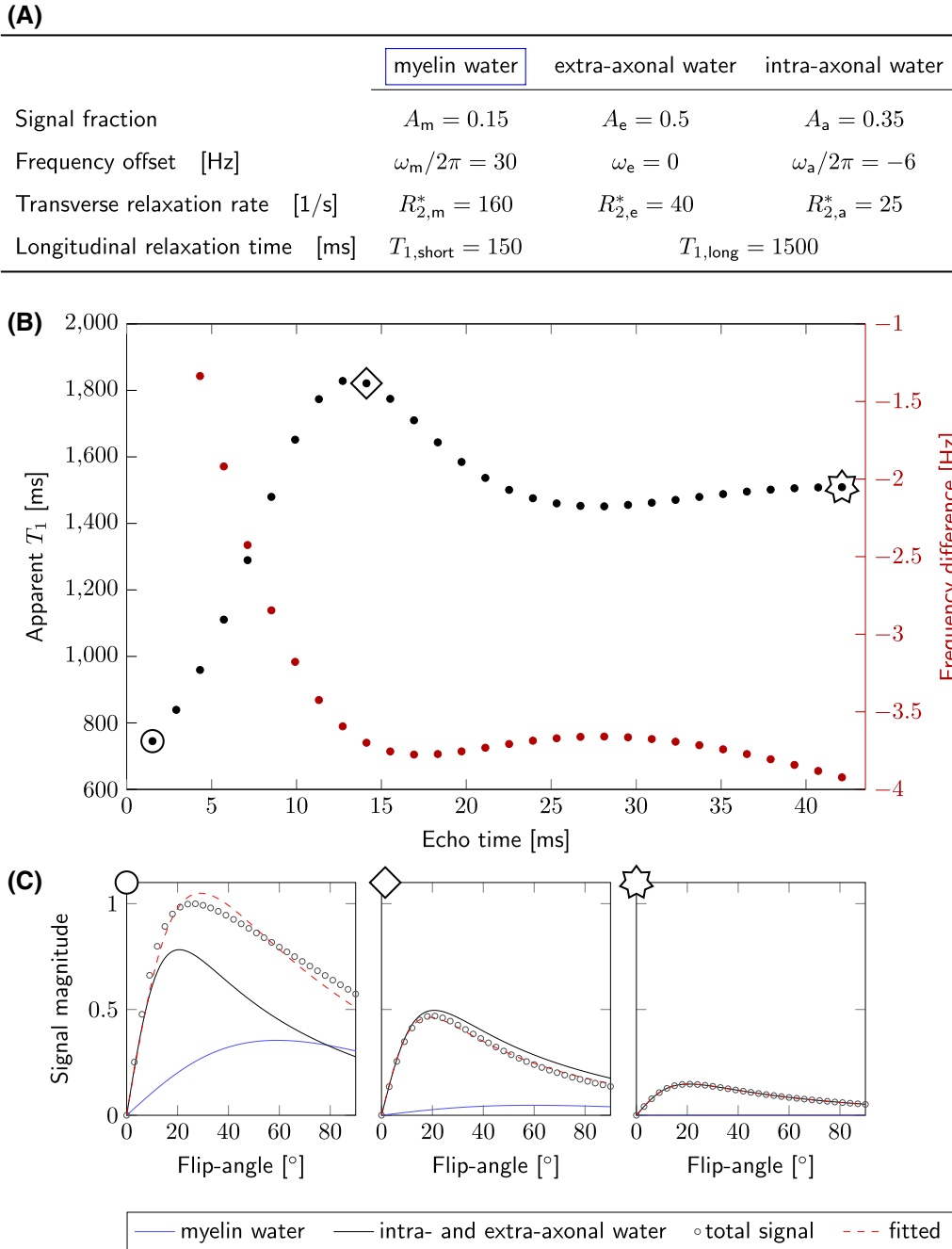


**FIGURE 1** Typical parameter values of the 3-pool model for nerve fibers oriented perpendicular to  $\vec{B}_0$  are listed in table (A),<sup>2,3,6,25</sup> along with short and long  $T_1$ -values.<sup>12</sup> The red plot in (B) shows evolution of the frequency difference with echo time estimated using values listed in the table (A). The black plot in (B) shows the apparent monoexponential  $T_1$ -values as a function of the echo time calculated by fitting Equation (6) to the total magnitude of the simulated 3-pool complex signal from a mGRE saturation-recovery experiment, assuming typical short and long  $T_1$ -values. Each plot in (C) corresponds to 1 of 3 echo times indicated in (B) and shows the variation of the magnitude of the complex signals from the myelin (short  $T_1$ ), intra- and extra-axonal (long  $T_1$ ) water, along with the total signal magnitude, as a function of flip angle at these echo times. The fit to the flip angle variation based on assuming the presence of a single  $T_1$  value at each echo time is shown using the dashed red line

possible RF excitation pulse that could be used to achieve 80° flip angle on the scanner. The RF pulse amplitudes were then scaled by 1.00, 0.75, 0.60, 0.45, 0.30, and 0.10 to produce nominal flip angles of 80°, 60°, 48°, 36°, 24°, and 8°.  $B_1^+$ -amplitude variation was adopted over varying the pulse duration because it allowed us to avoid variation of eddy current

effects due to variation of the strength and duration of the slice selection gradients. Thirty echoes were acquired for each excitation and the values of the first echo time, echo spacing, and repetition time were set to  $TE_1/\Delta TE/TR = 1.52/1.4/100$  ms. Magnitude, phase, real and imaginary images were saved for each echo time.

$B_1^+$ -maps were also acquired using a dual-TR, 3D gradient echo sequence<sup>26</sup> to allow the actual values of the excitation angles in the region of interest (ROI) to be determined. The values for flip angle, echo time, and first and second repetition times were  $\alpha/TE/TR_1/TR_2 = 60^\circ/5\text{ ms}/23\text{ ms}/80\text{ ms}$ , and the voxel size was  $3 \times 3 \times 5\text{ mm}^3$ .

In order to correct for residual eddy current-related field variation, mGRE data from a spherical phantom (outer diameter of 16 cm) containing aqueous copper sulfate solution were acquired for the same slice position and orientation as for the data acquired from each subject, using the same scanning parameters.

### 3.2 | Simulations

Complex mGRE signal evolution from intra-/extra-axonal and MW pools was simulated using Equation (7) combined with Equation (6) and using typical values for frequency offsets, transverse relaxation rates, signal fractions,<sup>3,6,25</sup> and longitudinal relaxation times.<sup>12,14</sup> These values are listed in the table in Figure 1A. Echo and repetition times were taken from the scanning parameters in this work, and flip angles ranged from  $0^\circ$  to  $90^\circ$ . The frequency difference was also calculated from the signal without  $T_1$ -weighting for demonstration of a typical frequency evolution as a function of time. Apparent monoexponential  $T_1$ -values as a function of echo time were estimated by fitting Equation (6) to the magnitude of the simulated 3-pool signal at each echo time under the assumption that a single  $T_1$  component was present.

### 3.3 | Data processing

Real and imaginary data were averaged across repeated scans for each echo time and combined to provide the complex signal evolution.

The product of the complex signals  $S_n^+$  and  $S_n^-$  was calculated for each RF excitation amplitude in order to remove the phase inconsistencies resulting from differences in the read gradient polarity along the echo train and then processed to generate frequency difference maps following Equation (3). Third-order spatially varying polynomial fits were estimated for each echo from the FDM phantom data and subtracted from the corresponding in vivo FDM data to correct for residual eddy current effects (see Figure S1 in Supporting Information). Finally, an ROI in the splenium of the corpus callosum was identified for each subject from the magnitude image acquired at a late echo time. The splenium of the corpus callosum was chosen as it is less susceptible to artifacts from the pulsatile blood flow in the anterior cerebral artery than the genu and body of the corpus callosum. This blood flow induces cardiac cycle-dependent phase shifts in the vessel

and thus voxel misregistration in the phase encoding direction which appear as ghosting of the vessel in FDM images, particularly at higher flip angles, as is evident in Figure 2F.

The mean values of the frequency difference and magnitude data were calculated for each echo in each dataset within the selected ROI. The absolute signal magnitude was fitted against  $M \cdot L(\alpha)$  for each echo time to estimate the echo time-dependent apparent monoexponential  $T_1$ -values. Here,  $M$  is a scaling constant and  $L(\alpha)$  is defined in Equation (6). The mGRE signal evolution was also jointly analyzed as a function of the echo time and the flip angle using the simple 3-pool model. Nonlinear least squares analysis was simultaneously performed on the frequency difference and magnitude data for all 6 amplitudes of the RF excitation pulses by modeling them using Equation (7).

All data analysis and computer simulations were performed in MATLAB<sup>®</sup> (MathWorks, Natick, MA).

## 4 | RESULTS

### 4.1 | Simulations

The red curve in Figure 1B shows a simulation of the temporal evolution of the frequency difference in a white matter region in which the nerve fibers are perpendicular to  $B_0$ . This was simulated using typical values for the frequency offsets, transverse relaxation rates and signal fractions of the intra-/extra-axonal and MW pools.<sup>2,3,6,25</sup> The black curve in Figure 1B shows the variation of the apparent monoexponential  $T_1$ -values as a function of echo time calculated by fitting to the signals simulated using previously reported short and long  $T_1$ -values in white matter.<sup>12</sup> Figure 1C shows how the magnitudes of the total signal and of the signals from the compartments with long and short  $T_1$ -values vary with flip angle at 3 different echo times. Figure 1C also shows the fit of the total signal magnitude variation with flip angle at the 3 different echo times. The fit is worst at the shortest echo time where the MW contribution to the signal is significant, but the  $R^2$  value is greater than 0.95 at all echo times.

### 4.2 | Preprocessing and example data

The example frequency difference maps in Figure 2 show the effect of changing the excitation pulse amplitude on the magnitude and FDM data measured at the echo time of 14 ms. They also show the effect on the frequency difference images of applying the correction for residual eddy current-related field variation using the data from the phantom. This process removes large length-scale variation of the frequency difference, making the local, tissue-related

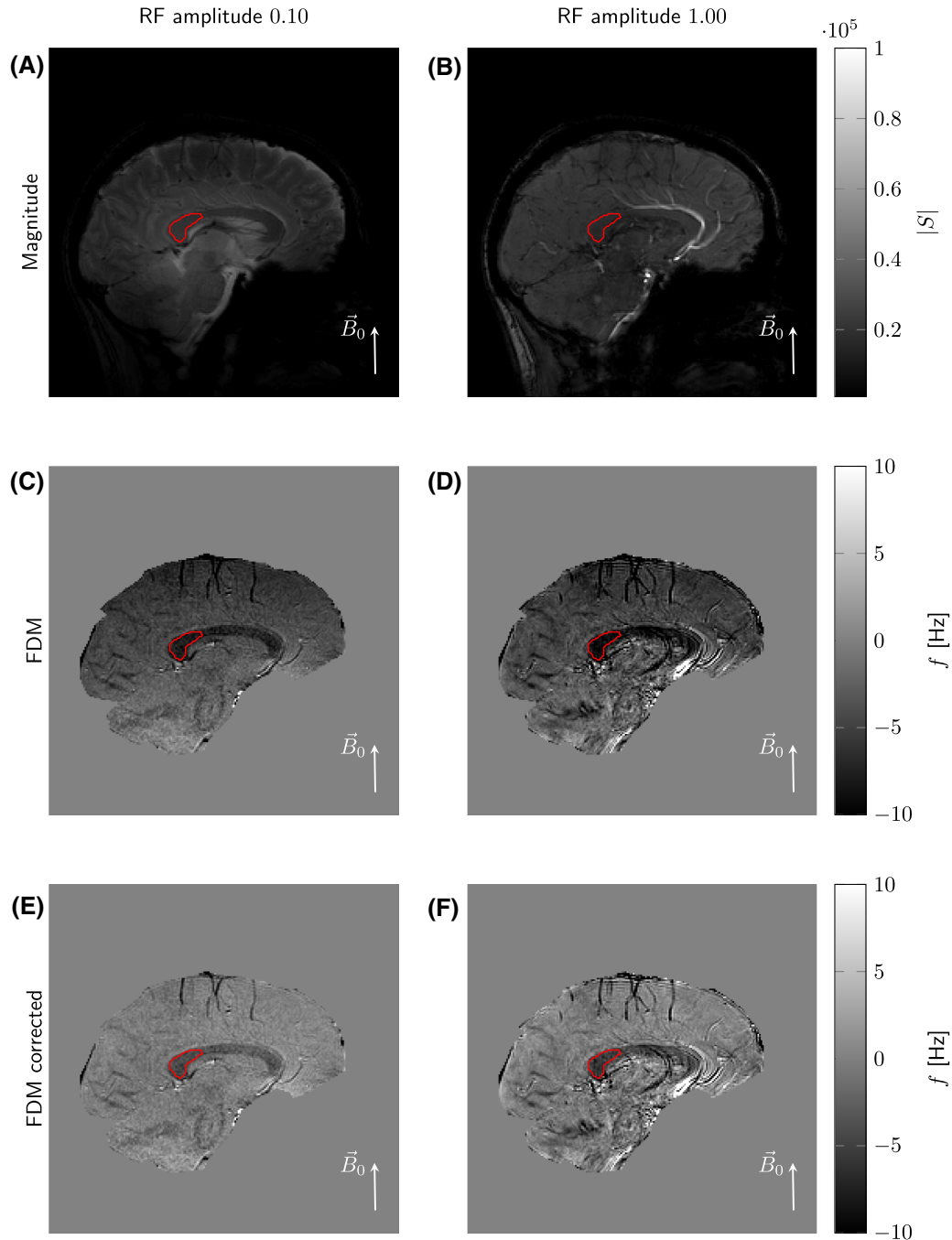


**FIGURE 2** Example magnitude images (A) and (B), frequency difference maps (C) and (D), and frequency difference maps corrected for eddy current effects (E) and (F) acquired at echo time of 14 ms. Data in (A), (C) and (E) were acquired at 10 % of the maximum  $B_1^+$ -amplitude, and data in (B), (D) and (F) were acquired at the maximum  $B_1^+$ -amplitude. Here, the maximum  $B_1^+$ -amplitude is associated with the amplitude of the shortest,  $80^\circ$  flip angle RF pulse. An ROI in the splenium of the corpus callosum is outlined in red in each image

effects more evident. The corpus callosum and veins are the regions which display the most significant local frequency variation and the largest difference in transverse relaxation rates across subvoxel compartments, and therefore are most prominent in the frequency difference map in Figure 2E. Figure 2F shows that the frequency difference contrast between the corpus callosum and surrounding tissue increases with increasing RF amplitude. The region of interest in the

splenium of the corpus callosum which was used for signal fitting is also indicated in this figure.

Figure 3 shows examples of phase data from the signals acquired using opposite read gradient polarities  $\arg(S_+)$  and  $\arg(S_-)$ , respectively, their quotient  $\arg(S_+/S_-)$  which shows the phase inconsistency between echoes acquired with different read gradient polarities, and their product  $\arg(S_+ \times S_-)$ , in which this inconsistency is eliminated.

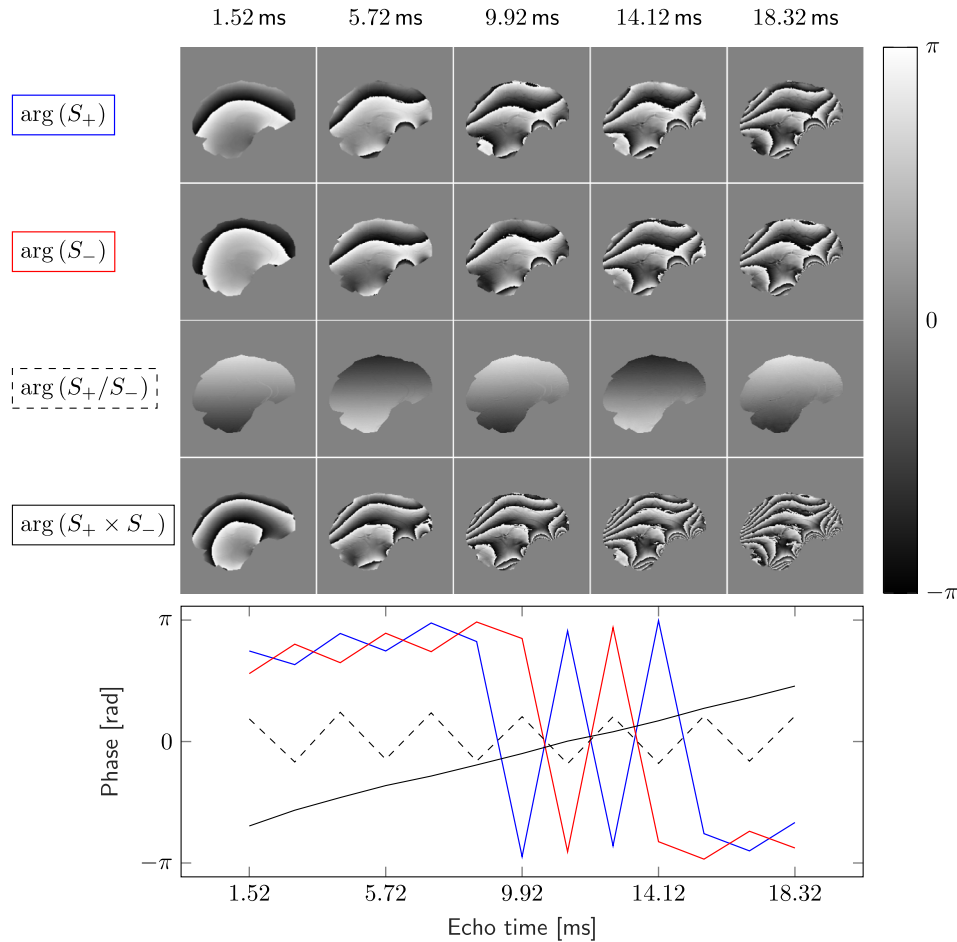


**FIGURE 3** The effect of the read gradient polarity on the mGRE phase data: the phase difference is calculated between the data acquired with opposite read gradient polarities (first and second rows) shows a clear phase inconsistency between the adjacent echoes (third row), which can be cancelled out by multiplying the complex signals acquired with opposite read gradient polarities (fourth row). The phase data from a voxel in the splenium of the corpus callosum are plotted as a function of echo time for  $S_+$  (blue),  $S_-$  (red),  $S_+/S_-$  (black dashed),  $S_+ \times S_-$  (black solid)

Figures 4 and 5 show the signal dependence on excitation angle (rows) and echo time (columns) for frequency difference and magnitude data, respectively, for 1 representative subject (Subject 5). Similar data for Subjects 1-4 are shown in Figures S2-S9 in Supporting Information. Increasing frequency difference contrast with increasing echo time and flip angle is evident. Supporting Information Figures S10 shows the  $B_1^+$  maps for each subject.

### 4.3 | Parameter estimation in the corpus callosum

Figure 6 shows the apparent  $T_1$ -values as a function of echo time estimated by fitting Equation (6) to the absolute magnitude values at each TE. The increase of apparent  $T_1$  with echo time in the first 10–15 ms is manifested in the data from all subjects and is consistent with the loss of a short  $T_1$

component over that period due to the fast  $T_2^*$ -decay of the MW signal. The magnitude of the variation of apparent  $T_1$  with echo time is however much smaller than that predicted from previously reported  $T_1$ -values for the slow and fast relaxing components<sup>12</sup> (c.f. black curve in Figure 1B).

Figure 7 shows frequency difference and magnitude data along with lines of best fit produced by joint fitting using Equation (7) in combination with Equation (6). Table 1 shows the individual fitting parameters estimated from each subject: frequency offsets  $f_a$  and  $f_m$ , transverse relaxation rates  $R_{2,a}^*$ ,  $R_{2,m}^*$  and  $R_{2,e}^*$ , short and long  $T_1$ -values, and the signal fractions  $c_m$ ,  $c_e$ , and  $c_a$ . The average and standard deviation over subjects of each of the fitted parameters is also shown. Additionally, Figure 8A compares the spread of short and long  $T_1$ -values across subjects. Figure 8B shows how the measured MW signal fraction is expected to vary with the flip angle, due to its shorter  $T_1$ . These plots were calculated using the fitted parameter values for each subject.

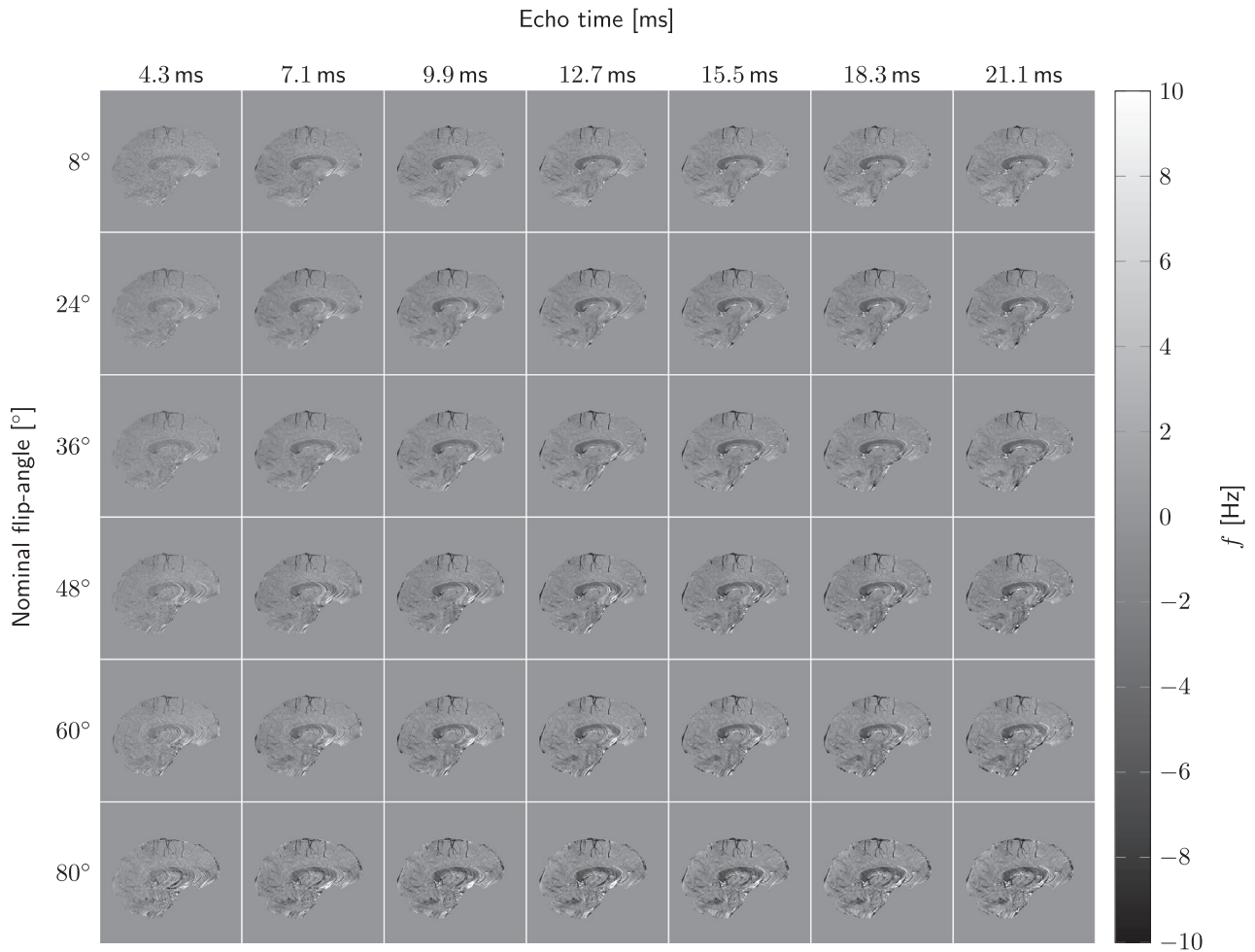


**FIGURE 4** Frequency difference dependence on the RF-pulse excitation angle (rows) and on the echo time (columns). Maps are shown for every other echo time from the 3rd to the 15th echo

## 5 | DISCUSSION

### 5.1 | Effect of variable excitation pulse on mGRE signal evolution

We observed that the apparent  $T_1$  estimated by fitting Equation (6) to the total signal magnitude at each gradient echo was smaller at short echo times TE (Figure 6). The increase in  $T_1$  as a function of TE occurred at a higher rate in the first 10 – 15 ms in all subjects. This increase is correlated with the rapid  $T_2^*$ -decay of the mGRE signal over the same time span, and with the increasing frequency difference manifested in Figure 7. For echo times above 15 ms, the apparent  $T_1$ -values were constant or slowly increasing. This behavior, which is consistent with the simulated data shown in Figure 1B indicates that the  $T_1$  of the short  $T_2^*$ , myelin-water pool is less than that of the long- $T_2^*$ , intra- and extra-axonal pools (Figure 8A). This finding is also consistent with previously reported work<sup>13,22</sup> and explains the increase of the measured frequency difference with flip angle which is evident in Figures 4 and 7.

The shorter  $T_1$  of the MW compared to that of the other water pools means that the MW signal is less strongly attenuated by saturation in short TR experiments. Consequently, the MW fraction will be overestimated by fitting to the gradient echo signal evolution. Figure 8B shows the predicted variation of the MW signal fraction with flip angle using the parameter values found by fitting to the signals from each subject (Table 1). These plots show that there would be on average a more than 30% overestimation of the MW fraction at the largest flip angle with a TR of 100 ms. This is consistent with recent observations by Shin et al<sup>22</sup>, who compared MW fraction estimated from mGRE data acquired with flip angles of 20° and 40° at a short repetition time of 70 ms.

Comparison of the experimentally measured (Figure 6) and simulated (Figure 1B) data indicates that although the apparent  $T_1$ -values were similar at the shortest TE, the observed increase in apparent  $T_1$  as a function of TE was much smaller than that estimated from the signal simulated using previously reported values of the relaxation times and relative volumes of the different compartments<sup>3,12</sup> (Figure 1).

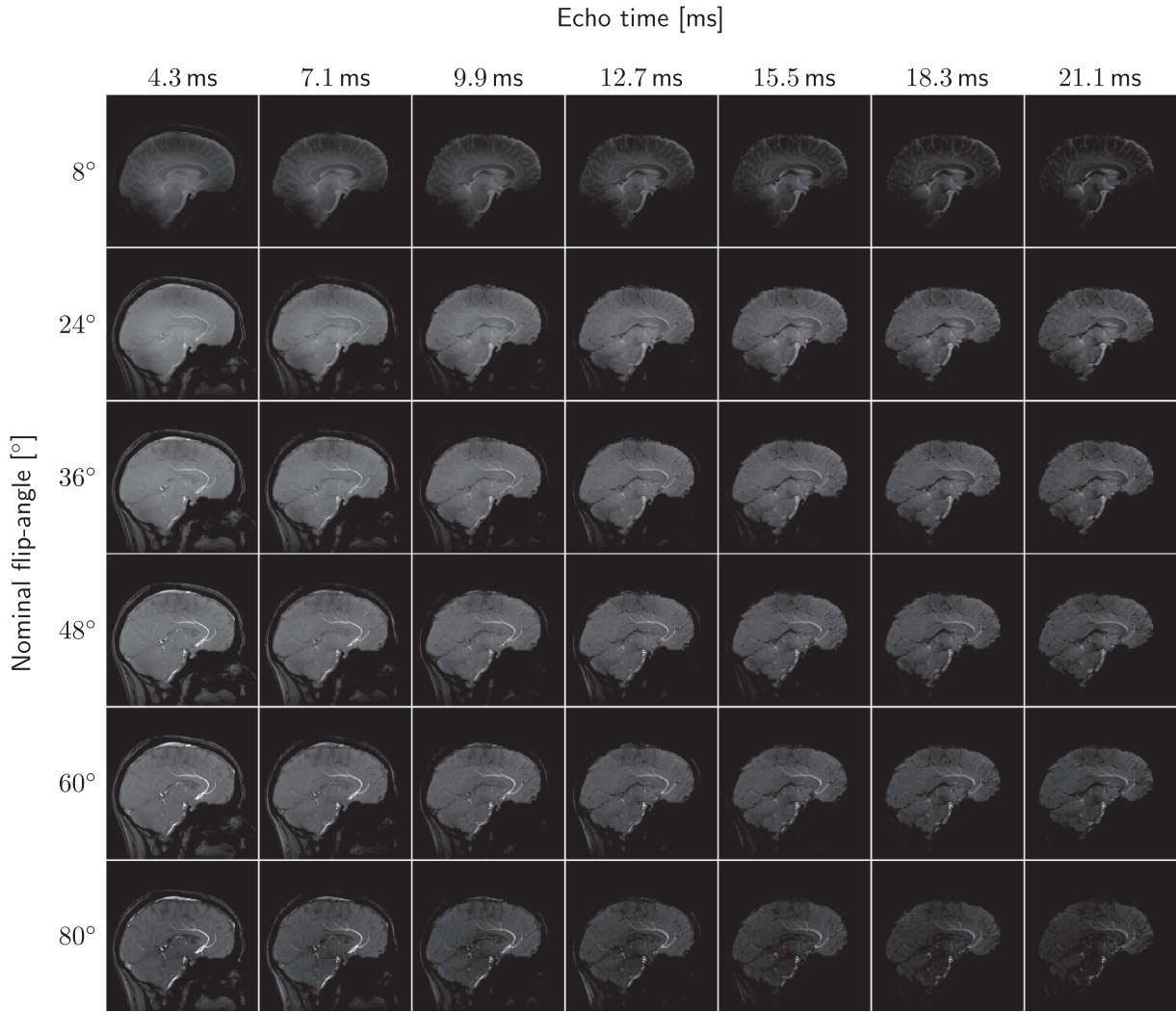


**FIGURE 5** Magnitude image dependence on the RF-pulse excitation angle (rows) and on the echo time (columns). Maps are shown for every other echo time from the 3rd to the 15th echo

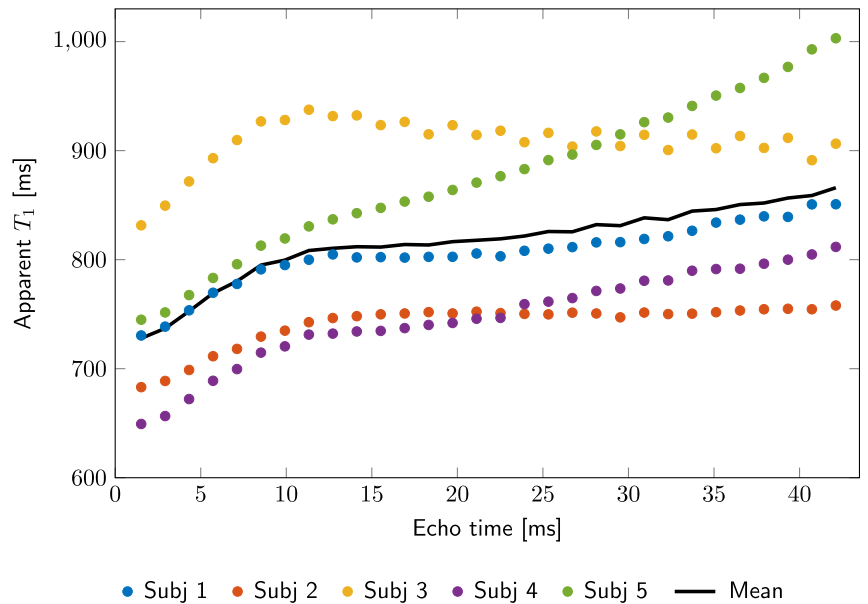


**FIGURE 6** Echo time-dependent apparent  $T_1$  estimated from the variation of the absolute magnitude values at each TE with  $\alpha$  for each subject

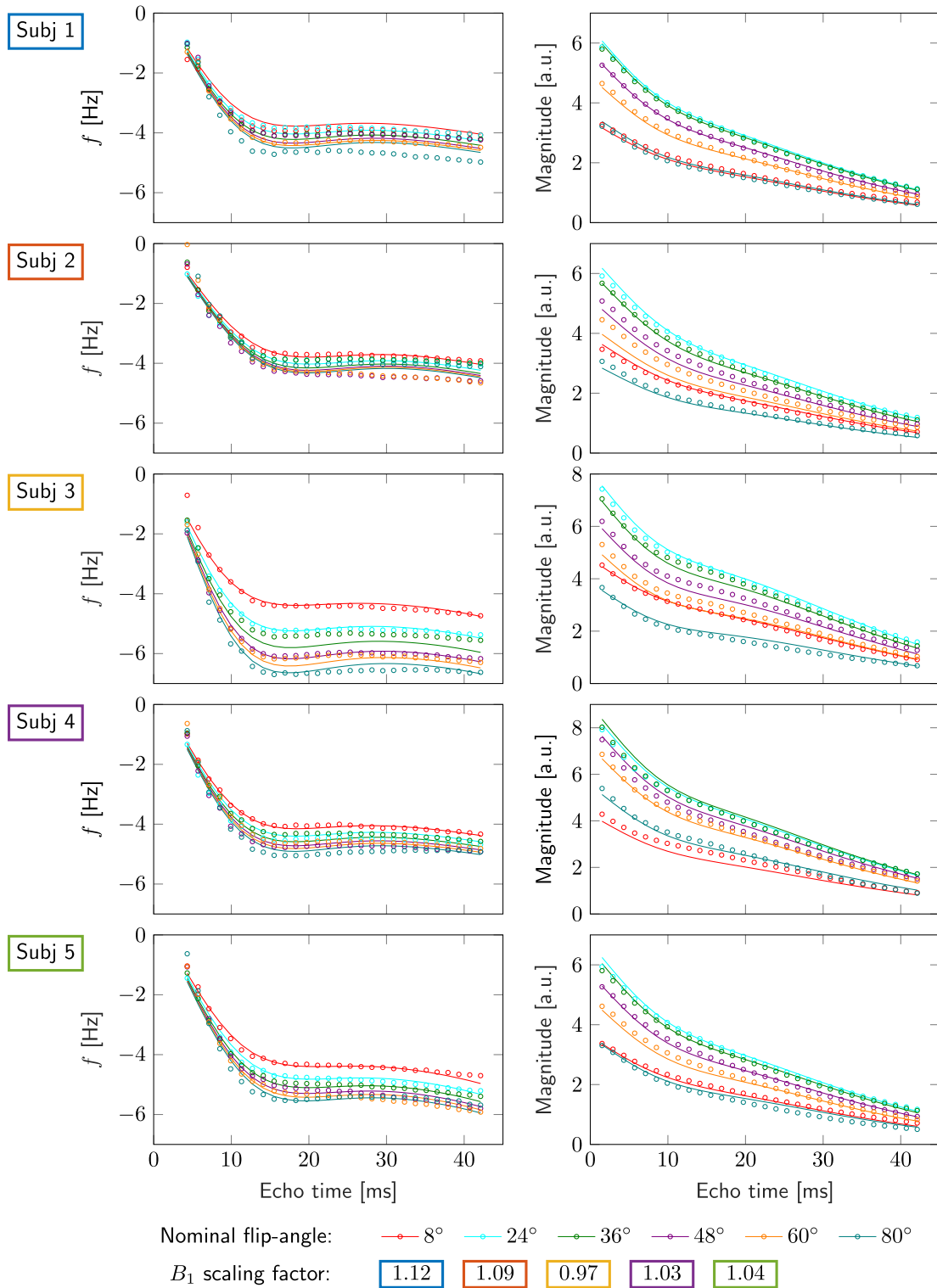


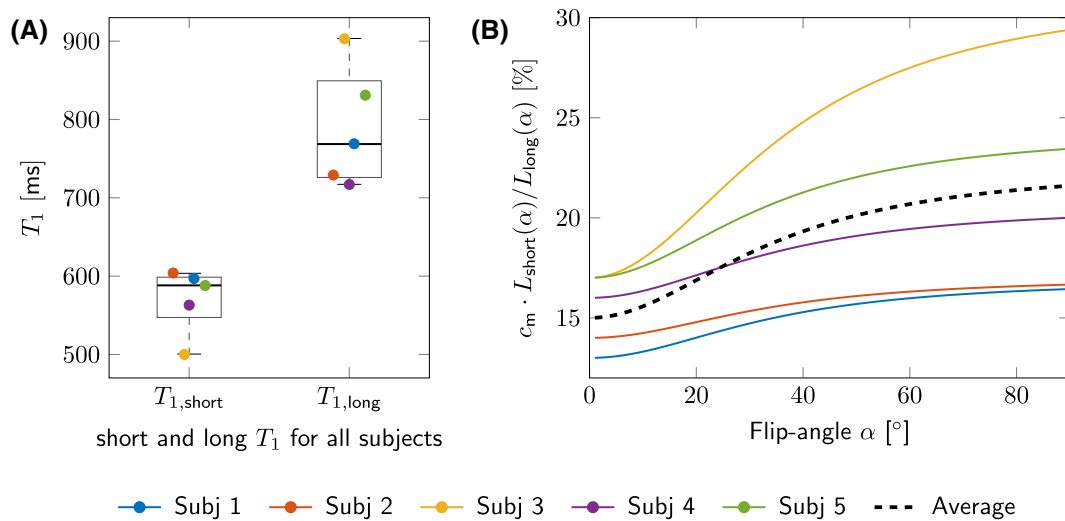
**FIGURE 7** Frequency difference and magnitude jointly fitted using Equation (7) to obtain short and long  $T_1$ -values. The actual flip angles used for each subject are given by multiplying the nominal flip angle by the  $B_1$  scaling factor which varied from 0.97 to 1.12

Similarly, the  $T_1$ -values of the short- and long- $T_2^*$  pools estimated from fitting the 3-pool model of the signal to the measured data ( $T_{1,short} = 500...604$  ms and  $T_{1,long} = 717...903$  ms) appear much closer to one another, than values resulting from inversion-recovery experiments

at 7T7T.<sup>12,16</sup> Labadie et al<sup>12</sup>  $T_1$  peak (= 106...225 ms) and a long- $T_1$  peak (= 1500...1660 ms) in a  $T_1$  relaxogram and Rioux et al<sup>16</sup> reported short  $T_1 = 57$  ms and long  $T_1 = 1349$  ms resulting from fitting a bi-exponential to their data. Interestingly, Van Gelderen and Duyn<sup>11</sup> suggested that

**TABLE 1** Frequency offsets, relaxation rates, and apparent  $T_1$ -values of the short and long  $T_2^*$ -components, obtained from the fits in Figure 7 for each subject

	Frequency offsets (Hz)		Transverse relaxation (1/s)			Longitudinal relaxation (ms)		Signal fractions (%)		
	$f_a$	$f_m$	$R_{2,m}^*$	$R_{2,e}^*$	$R_{2,a}^*$	$T_{1,short}$	$T_{1,long}$	$c_m$	$c_e$	$c_a$
Subject 1	$-7.1 \pm 0.9$	$32.0 \pm 2.0$	$137 \pm 5$	$35 \pm 1$	$7 \pm 19$	$597 \pm 13$	$769 \pm 14$	13	72	15
Subject 2	$-6.9 \pm 0.7$	$28.7 \pm 2.9$	$128 \pm 5$	$34 \pm 2$	$11 \pm 19$	$604 \pm 14$	$729 \pm 13$	14	66	20
Subject 3	$-8.5 \pm 0.2$	$29.1 \pm 2.1$	$153 \pm 5$	$23 \pm 2$	$0 \pm 7$	$500 \pm 9$	$903 \pm 12$	17	63	20
Subject 4	$-7.3 \pm 0.6$	$29.5 \pm 2.5$	$149 \pm 6$	$30 \pm 1$	$5 \pm 15$	$563 \pm 11$	$717 \pm 11$	16	67	16
Subject 5	$-7.7 \pm 0.2$	$27.5 \pm 2.1$	$144 \pm 4$	$31 \pm 2$	$8 \pm 10$	$588 \pm 10$	$831 \pm 11$	17	61	22
Average	$-7.5 \pm 0.6$	$29.4 \pm 1.6$	$142 \pm 10$	$34 \pm 5$	$6 \pm 4$	$570 \pm 42$	$844 \pm 70$	$15 \pm 2$	$66 \pm 4$	$19 \pm 3$

**FIGURE 8** (A) The apparent short and long  $T_1$ -values estimated from the fits in Figure 7. (B) The myelin water signal fraction is expected to vary as a function of the flip angle, based on the differences in saturation between the myelin water, and intra-/extra-axonal water

the combined semi-solid/myelin-water  $T_1$  is about 530 ms, which agrees with our  $T_{1,short}$ -values. In their work Van Gelderen and Duyn<sup>11</sup> combined an mGRE experiment with various preparation pulses to vary the relative states of the magnetization in the semi-solid and water pools in WM. They then modeled the magnetization in each compartment using a set of Bloch equations which incorporate magnetization exchange between water pools and myelin sheath layers. One of their main conclusions was that the exchange between the MW and the intra-/extra-axonal pools is too fast to separately measure their  $T_1$ -values. Fast exchange between short- and long- $T_2^*$  water pools could have led to identification of less distinct  $T_{1,short}$ - and  $T_{1,long}$ -values in this saturation-recovery experiment compared to the previous inversion-recovery experiments.<sup>12,16</sup> Additionally, Ou and Gochberg<sup>27</sup> suggested that on-resonance saturation of the macro-molecular pool leads to an RF-amplitude-dependent (and thus flip angle-dependent) reduction of the steady-state signal in saturation-recovery measurements and, as a result, an underestimation of the apparent  $T_1$  when assuming there is a single-pool in fitting the data

(in contrast to a 2-pool system consisting of free water pool and macro-molecular water pool that incorporates the effect of magnetization transfer). In our experiment, we used a relatively short, fixed TR of 100 ms and varied the flip angle of the excitation RF-pulse by modulating its amplitude. As a result, we measure apparent  $T_1$ -values of less than 1 second for all echo times. These are more than 20% lower than the generally reported value of  $T_1$  in white matter.<sup>28</sup> Finally, Barta et al<sup>17</sup> have questioned the accuracy of multicomponent  $T_1$  analysis in white matter. In particular, their results suggested that the short  $T_1$ -component cannot be solely associated with MW pools, as it also might contain the contribution of intra-/extra-axonal water components exchanging with macromolecules.

## 5.2 | Limitation of simple 3-pool model

We estimated  $T_1$ -values from the mGRE saturation-recovery data by simultaneously fitting the echo time and flip angle dependence of the signal magnitude and frequency difference

to a simple 3-pool model. Although this model captures the differences in the  $T_1$ -values of the short and long  $T_2^*$  pools, it does not seem to characterize the full behavior of the saturation-recovery signal. This is evident from the relative poorness of the fits shown in Figure 7. By increasing the weighting of the frequency difference data in the fitting process, it was possible to improve the fits to the FDM curves, but this came at the expense of worse fitting of the magnitude signals. This most likely indicates that the 3-pool model used here is too simplistic and needs to be modified to include the effects of exchange between compartments and of magnetization transfer involving a macromolecular compartment that does not generate a measurable signal at the echo times used here. The model could also be improved by incorporating the effects of fiber orientation dispersion.<sup>29</sup> In general, the fitting parameters shown in Table 1 are in reasonable agreement with previous reported values,<sup>2,3,6,25</sup> but the estimated size of the signal from the external compartment relative to the axonal compartment is significantly larger than previous data. This might be indicative of greater exchange between the MW and external pool (compared to the axonal pool), but further experimentation and modeling would be needed to explore this idea. In addition, the fitted value of  $R_{2,a}^*$  was significantly smaller than previous reports.

We evaluated the sensitivity of the fitting parameters to noise propagation, by fitting to magnitude and frequency difference data calculated from the complex signal formed using the 3-pool model in Equation (7) and the average parameter values reported in Table 1. Random Gaussian noise was added to the real and imaginary signals to yield a representative SNR of 50, and the signals from 10 repeats were averaged together before fitting, as in the experiment. This process was repeated 100 times and the average and standard deviation of the fitted parameters are reported in Table S1 and an example fit is shown in Figure S13. These results do not show strong systematic deviations of the fitted parameter values from the input values to the simulations, and show reasonable levels of precision. This suggests that propagation of the effects of random noise alone is not responsible for the relatively poor model fitting seen in Figure 7, but rather there is a systematic difference between the model predictions and the experimental data.

### 5.3 | Complex signal pre-processing

Correction of phase inconsistencies between adjacent echoes by means of multiplying complex signals acquired with opposite readout polarities allowed us to acquire FDM data using a bipolar gradient echo readout. This provided a smaller echo spacing than can be achieved using a monopolar readout and hence a better characterization of the temporal evolution of the complex signal. Echo spacing could be further decreased,

but only at a cost of reduced spatial resolution. FDM allows only for correction of zeroth- and first-order temporal field perturbations, that is, RF related phase offsets and the effect of  $B_0$  perturbations. Temporal evolution of short-lived, eddy current-related field variations is usually represented as a superposition of multiple exponential decays and thus cannot be fully accounted for in the FDM processing.

However, eddy current effects are purely hardware dependent and thus are independent of the object placed in the magnet. This allowed us to characterize the eddy current effects by carrying out FDM on a uniform phantom and then to subtract them from the brain measurements. Since the eddy current effects are spatially slowly varying they could be approximated using low-degree spatial polynomials. Using polynomials to characterize the eddy current effects meant that the subtraction produced a lesser reduction in the SNR of the frequency difference maps and also allowed extension of the eddy current estimates to cover brain regions which lay outside the extent of the 16 cm-diameter phantom.

The advantage of this method compared with data-based approach, for example, fitting a low-degree polynomial to the *in vivo* data,<sup>6</sup> is the reduced likelihood of fitting to and then subtracting phase contrast induced due by the microstructural features of interest. However, this method does rely on invariance of the eddy current effects over a long experimental acquisition, which might be compromised by changes in the gradient coil temperature. Simultaneous use of a dynamic field camera system might help us to address these challenges.<sup>30</sup>

### 5.4 | $T_1$ estimation and the nonuniform slice excitation

One potential source of error in  $T_1$  estimation from the 2-dimensional acquisition is the effect of the nonuniformity of the excitation,<sup>31-33</sup> which results in the transverse magnetization varying across the slice thickness (Supporting Information Figure S11a). The variation of flip angle  $\alpha(x)$  across the slice is shown in Supporting Information Figure S11b for different nominal flip angles. The assumption made in our work is that the signal dependence on RF amplitude is well characterized by using a flip angle measure formed by scaling the average flip angle measured over the slice at 1 RF amplitude. Supporting Information Figure S11c shows good agreement between the nominal and the averaged-through-slice true excitation angles. Additionally, we tested whether the assumption that the signal as a function of averaged excitation angle  $S(\langle\alpha(x)\rangle_{\text{slice}})$  delivers a good approximation to the actual signal averaged over the full slice profile  $S = \langle s(\alpha(x)) \rangle_{\text{full slice profile}}$ . To do this, the  $T_1$ -values (Figure 8B) estimated under the assumption  $S = S(\langle\alpha\rangle_{\text{slice}})$  were substituted into  $S = \langle s(\alpha(x)) \rangle_{\text{full slice profile}}$ . In Supporting

Information Figure S12, the measured normalized signal is compared to signal calculated using the  $T_1$ . There is no significant difference between the actual and the simulated signals.

## 5.5 | Vascular ghosting

The pulsatile blood flow in the imaging plane in the anterior cerebral artery caused ghosting artifacts in the phase encoding direction, as is visible in Figure 2F. The effect is stronger in the data acquired with a higher excitation angle due to the higher signal of the arterial blood relative to the surrounding tissue; for example, in the magnitude data in Figure 2B, the artery appears to be much brighter than the surrounding tissue in comparison to the lowest excitation angle magnitude data in Figure 2A. The artifact decreases with the increasing distance from the artery, and hence, the splenium of the corpus callosum was selected for detailed analysis.

Flow compensation gradients<sup>21,34</sup> or in-flow signal suppression<sup>24</sup> could be used to reduce this artifact. The flow compensation gradients are usually placed before the read gradients, which comes at a cost of a longer first echo time and is therefore not advisable for detection of the fast-decaying MW signal at 7 T. In-flow signal saturation prior to the excitation pulse may induce unwanted slice profile modulation and incidental MT effects.

## 6 | CONCLUSION

The MW mGRE signal decays at a much faster rate than the intra- and extra-axonal signals, making the mGRE sequence a useful tool for estimation of the MW fraction as an indirect measure of myelination.<sup>2,3,6,13,14,23-25</sup> Using in vivo 7T measurements of the signal from the splenium of the corpus callosum, we have demonstrated that the relative amplitudes of the short and long  $T_2^*$  signals in white matter can be modulated by varying the  $B_1^+$  amplitude in a saturation-recovery mGRE sequence. This behavior means that the MW signal makes a larger relative contribution to the signal at higher levels of saturation and the MW fraction may consequently be overestimated. It also leads to variation with echo time of the apparent  $T_1$ , found by fitting the signal variation with flip angle to a single component  $T_1$  model. The observed relative signal modulation and variation of  $T_1$  with flip angle is however less than that predicted using the compartmental  $T_1$ -values estimated from inversion recovery experiments.<sup>12,16</sup>

We also incorporated  $T_1$ -weighting into the simple 3-pool model of white matter and used the resulting expressions in a joint fit of the variation of signal magnitude and frequency difference with flip angle and echo time. The short and long  $T_1$  values found from the fits deviate from

previous measurements, being more similar to one another, and although the other fitting parameters are similar to those found previously using the 3-pool model, it proved difficult to fit both the magnitude and frequency difference simultaneously. This suggests that the 3-pool model needs to be extended to include the effects of exchange and magnetization transfer for proper characterization of the signal evolution. Careful investigations of the mechanisms underlying this behavior and their sensitivity to the sequence parameters will be crucial for the accurate estimation of the MW fraction.<sup>35</sup>

## ORCID

Elena Kleban <http://orcid.org/0000-0002-9814-0807>

## TWITTER

Richard Bowtell  @SPMIC\_UoN  @richardbowtell

## REFERENCES

- Weiger M, Froidevaux R, Baadsvik EL, Brunner DO, Rösler MB, Pruessmann KP. Advances in MRI of the myelin bilayer. *NeuroImage*. 2020;217:116888.
- Wharton S, Bowtell R. Fiber orientation-dependent white matter contrast in gradient echo MRI. *Proc Nat Acad Sci*. 2012;109:18559-18564.
- Sati P, van Gelderen P, Silva AC, Reich DS, Merkle H, de Zwart JA, et al. Micro-compartment specific  $T_2^*$  relaxation in the brain. *NeuroImage*. 2013;77:268-278.
- Wharton S, Bowtell R. Effects of white matter microstructure on phase and susceptibility maps. *Magn Reson Med*. 2015;73:1258-1269.
- Sood S, Urriola J, Reutens D, O'Brien K, Bollmann S, Barth M, et al. Echo time-dependent quantitative susceptibility mapping contains information on tissue properties. *Magn Reson Med*. 2017;77:1946-1958.
- Tendler BC, Bowtell R. Frequency difference mapping applied to the corpus callosum at 7T. *Magn Reson Med*. 2019;81:3017-3031.
- Pampel A, Müller DK, Anwander A, Marschner H, Müller HE. Orientation dependence of magnetization transfer parameters in human white matter. *NeuroImage*. 2015;114:136-146.
- Schyboll F, Jaekel U, Weber B, Neeb H. The impact of fibre orientation on  $T_1$ -relaxation and apparent tissue water content in white matter. *Magn Reson Mater Phys, Biol Med*. 2018;31:501-510.
- Schyboll F, Jaekel U, Petruccione F, Neeb H. Fibre-orientation dependent  $R_1$  ( $= 1/T_1$ ) relaxation in the brain: the role of susceptibility induced spin-lattice relaxation in the myelin water compartment. *J Magn Reson*. 2019;300:135-141.
- Schyboll F, Jaekel U, Petruccione F, Neeb H. Dipolar induced spin-lattice relaxation in the myelin sheath: a molecular dynamics study. *Sci Rep*. 2019;9.
- vanGelderen P, Duyn JH. White matter intercompartmental water exchange rates determined from detailed modeling of the myelin sheath. *Magn Reson Med*. 2019;81:628-638.
- Labadie C, Lee JH, Rooney WD, Jarchow S, Aubert-Frécon M, Springer CS, et al. Myelin water mapping by spatially regularized longitudinal relaxographic imaging at high magnetic fields. *Magn Reson Med*. 2014;71:375-387.

13. Oh SH, Bilello M, Schindler M, Markowitz CE, Detre JA, Lee J. Direct visualization of short transverse relaxation time component (ViSta). *NeuroImage*. 2013;83:485-492.
14. Kim D, Lee HM, Oh SH, Lee J. Probing signal phase in direct visualization of short transverse relaxation time component (ViSta). *Magn Reson Med*. 2015;74:499-505.
15. vanGelderens P, Jiang X, Duyn JH. Effects of magnetization transfer on  $T_1$  contrast in human brain white matter. *NeuroImage*. 2016;128:85-95.
16. Rioux JA, Levesque IR, Rutt BK. Biexponential longitudinal relaxation in white matter: characterization and impact on  $T_1$  mapping with IR-FSE and MP2RAGE. *Magn Reson Med*. 2016;75:2265-2277.
17. Barta R, Kalantari S, Laule C, Vavasour IM, MacKay AL, Michal CA. Modeling  $T_1$  and  $T_2$  relaxation in bovine white matter. *J Magn Reson*. 2015;259:56-67.
18. Yu H, Shimakawa A, McKenzie CA, Lu W, Reeder SB, Hinks RS, et al. Phase and Amplitude Correction for Multi-Echo Water-Fat Separation With Bipolar Acquisitions. *J Magn Reson Imaging*. 2010;31:1264-1271.
19. Hargreaves B, Lu W. Magnetic Resonance Imaging with bipolar multi-echo sequences. <http://www.freepatentsonline.com/7777486.html> 2010.
20. Peterson P, Månsson S. Fat quantification using multiecho sequences with bipolar gradients: investigation of accuracy and noise performance. *Magn Reson Med*. 2014;71:219-229.
21. Lee H, Nam Y, Lee HJ, Hsu JJ, Henry RG, Kim DH. Improved three-dimensional multi-echo gradient echo based myelin water fraction mapping with phase related artifact correction. *NeuroImage*. 2018;169:1-10.
22. Shin HG, Oh SH, Fukunaga M, Nam Y, Lee D, Jung W, et al. Advances in gradient echo myelin water imaging at 3T and 7T. *NeuroImage*. 2019;188:835-844.
23. vanGelderens P, de Zwart JA, Lee J, Sati P, Reich DS, Duyn JH. Nonexponential  $T_2^*$  decay in white matter. *Magn Reson Med*. 2012;67:110-117.
24. Nam Y, Lee J, Hwang D, Kim DH. Improved estimation of myelin water fraction using complex model fitting. *NeuroImage*. 2015;116:214-221.
25. Thapaliya K, Vegh V, Bollmann S, Barth M. Assessment of microstructural signal compartments across the corpus callosum using multi-echo gradient recalled echo at 7T. *NeuroImage*. 2018;182:407-416.
26. Yarnykh VL. Actual flip-angle imaging in the pulsed steady state: a method for rapid three-dimensional mapping of the transmitted radiofrequency field. *Magn Reson Med*. 2007;57:192-200.
27. Ou X, Gochberg DF. MT effects and  $T_1$  quantification in single-slice spoiled gradient echo imaging. *Magn Reson Med*. 2008;59:835-845.
28. Wright P, Mougins O, Totman J, Peters A, Brookes M. Water proton  $T_1$  measurements in brain tissue at 7, 3, and 1.5 T using IR-EPI, IR-TSE, and MPRAGE: results and optimization. *Magn Reson Mater Phy*. 2008;21:121-130.
29. Xu T, Foxley S, Kleinnijenhuis M, Chen WC, Miller KL. The effect of realistic geometries on the susceptibility-weighted MR signal in white matter. *Magn Reson Med*. 2018;79:489-500.
30. Vannesjo SJ, Haeberlin M, Kasper L, Pavan M, Wilm BJ, Barmet C, et al. Gradient system characterization by impulse response measurements with a dynamic field camera. *Magn Reson Med*. 2013;69:583-593.
31. Parker GJM, Barker GJ, Tofts PS. Accurate multislice gradient echo  $T_1$  measurement in the presence of non-ideal RF pulse shape and RF field nonuniformity. *Magn Reson Med*. 2001;45:838-845.
32. Svedin BT, Parker DL. Technical note: the effect of 2D excitation profile on  $T_1$  measurement accuracy using the variable flip angle method with an average flip angle assumption. *Med Phys*. 2017;44:5930-5937.
33. Stikov N, Boudreau M, Levesque IR, Tardif CL, Barral JK, Pike GB. On the accuracy of  $T_1$  mapping: searching for common ground. *Magn Reson Med*. 2015;73:514-522.
34. Xu B, Liu T, Spincemaille P, Prince M, Wang Y. Flow compensated quantitative susceptibility mapping for venous oxygenation imaging. *Magn Reson Med*. 2013;72:438-445.
35. Chan KS, Marques JP. Multi-compartment relaxometry and diffusion informed myelin water imaging – Promises and challenges of new gradient echo myelin water imaging methods. *Neuroimage*. 2020;221:117159. <http://dx.doi.org/10.1016/j.neuroimage.2020.117159>.

## SUPPORTING INFORMATION

Additional Supporting Information may be found online in the Supporting Information section.

**FIGURE S1** Examples of A, FDM calculated from the phantom data, B, a third degree polynomial fit to the data and C, The residual resulting from subtracting the fit from the data. Profiles show the variation of frequency difference with z-coordinate along the line marked on the maps

**FIGURE S2** Subject 1: FDM as a function of the RF-pulse amplitude (rows) and the echo time (columns). Maps are shown for every other echo time from the 3rd to the 15th echo. An RF amplitude scale of 1 corresponds to a nominal angle of  $80^\circ$

**FIGURE S3** Subject 2: FDM as a function of the RF-pulse amplitude (rows) and the echo time (columns). Maps are shown for every other echo time from the 3rd to the 15th echo. An RF amplitude scale of 1 corresponds to a nominal angle of  $80^\circ$

**FIGURE S4** Subject 3: FDM as a function of the RF-pulse amplitude (rows) and the echo time (columns). Maps are shown for every other echo time from the 3rd to the 15th echo. An RF amplitude scale of 1 corresponds to a nominal angle of  $80^\circ$

**FIGURE S5** Subject 4: FDM as a function of the RF-pulse amplitude (rows) and the echo time (columns). Maps are shown for every other echo time from the 3rd to the 15th echo. An RF amplitude scale of 1 corresponds to a nominal angle of  $80^\circ$

**FIGURE S6** Subject 1: Magnitude data as a function of the RF-pulse amplitude (rows) and the echo time (columns). Maps are shown for every other echo time from the 3rd to the 15th echo. An RF amplitude scale of 1 corresponds to a nominal angle of  $80^\circ$

**FIGURE S7** Subject 2: Magnitude data as a function of the RF-pulse amplitude (rows) and the echo time (columns).

Maps are shown for every other echo time from the 3rd to the 15th echo. An RF amplitude scale of 1 corresponds to a nominal angle of  $80^\circ$

**FIGURE S8** Subject 3: Magnitude data as a function of the RF-pulse amplitude (rows) and the echo time (columns). Maps are shown for every other echo time from the 3rd to the 15th echo. An RF amplitude scale of 1 corresponds to a nominal angle of  $80^\circ$

**FIGURE S9** Subject 4: Magnitude data as a function of the RF-pulse amplitude (rows) and the echo time (columns). Maps are shown for every other echo time from the 3rd to the 15th echo. An RF amplitude scale of 1 corresponds to a nominal angle of  $80^\circ$

**FIGURE S10**  $B_1^+$  maps were acquired using a dual-TR, 3D gradient echo sequence. Here, the masked maps are overlaid on the magnitude data for each subject.

**FIGURE S11** A,  $M_x^-$ ,  $M_y^-$ , and  $M_z^-$ -components of magnetisation as a function of position following application of a nominal  $80^\circ$  flip angle pulse and 5mm slice thickness. B, Excitation angle variation through the slice  $\alpha(z)$  (solid lines) and the nominal excitation angle  $\alpha_{\text{nominal}}$  (dashed lines). C, Good agreement between the nominal excitation angle and the true excitation angle averaged across the slice

**FIGURE S12** Comparison between the experimental values and the values calculated based on the estimated  $T_1$  and the slice profiles as described in Equation (S1)

**TABLE S1** Signal evolution as a function of echo time and flip angle was simulated using the model in Equation (7) and the values in row “Input”. Complex signals were perturbed by addition of Gaussian random noise to the real and imaginary signal components yielding SNR = 50 and averaged over 10 perturbation repeats. The signal magnitude and frequency difference evolution were then calculated and fitted 100 times using the model in Equation (7) to estimate the uncertainty of the fitted values: resulting mean and standard deviations are listed in row “Fitted”

**FIGURE S13** Noise propagation: example for simulated FDM and magnitude data using SNR = 50

**How to cite this article:** Kleban E, Gowland P, Bowtell R. Probing the myelin water compartment with a saturation-recovery, multi-echo gradient-recalled echo sequence. *Magn Reson Med.* 2021;86: 167–181. <https://doi.org/10.1002/mrm.28695>